NUMERICAL STUDY ON THE FORMATION OF A BULGING REGION IN PARTIAL PENETRATION LASER BEAM WELDING

A. ARTINOV*, X. MENG*, M. BACHMANN*, M. RETHMEIER**,*,***

*Bundesanstalt für Materialforschung und -prüfung (BAM), Unter den Eichen 87, 12205 Berlin, Germany
**Institute of Machine Tools and Factory Management, Technische Universität Berlin, Pascalstraße 8-9, 10587 Berlin, Germany
***Fraunhofer Institute for Production Systems and Design Technology, Pascalstraße 8-9, 10587 Berlin, Germany

ABSTRACT

A transient three-dimensional thermo-fluid dynamics numerical model was developed to study the formation of a bulging region in partial penetration laser beam welding. The model accounts for the coupling between the fluid flow, the heat transfer, and the keyhole dynamics by considering the effects of multiple reflections and Fresnel absorption of the laser beam in the keyhole, the phase transitions during melting and evaporating, the thermo-capillary convection, the natural convection, and the phase-specific and temperature-dependent material properties up to the evaporation temperature. The validity of the model was backed up by experimentally obtained data, including the drilling time, the weld pool length, the local temperature history outside the weld pool, the process efficiency, and a range of metallographic cross-sections. The model was applied for the cases of partial penetration laser beam welding of 8 mm and 12 mm thick unalloyed steel sheets. The obtained experimental and numerical results reveal that the bulging region forms transiently depending on the penetration depth of the weld, showing a tendency to transition from a slight bulging to a fully developed bulging region between penetration depths of 6 mm and 9 mm, respectively.

Keywords: Laser beam welding, Deep penetration, Bulge formation, Numerical modeling

INTRODUCTION

In recent years, modern laser systems with high power of up to 100 kW for solid state lasers have been developed, offering a number of technical benefits compared to traditional arc welding techniques, including reduced distortion of the welded components due to locally highly concentrated and precise heat input, high reachable welding speed, a small heat affected zone [4], and enabling single pass welding of sheets with a thickness of up to 50 mm [1–3]. As a result, many new opportunities for applications open up for joining thicker sheets by the laser beam welding technique, e.g., in the manufacturing of high-pressure and vacuum vessels, crane constructions, shipbuilding, and aerospace industry. Nevertheless, as welding speed and sheet thickness increase, new challenges and

issues emerge, such as the formation of non-common defects for specific materials, such as hot-cracking during welding of unalloyed and low-alloyed steels [5–7]. Even though hot-cracking is one of the most researched material phenomena in welding, its nature remains complex [8,9]. However, it is well recognized nowadays that the interplay of three main factors is critical for the welded specimens' susceptibility to cracking, namely the thermal, mechanical, and metallurgical factor [10]. Thereby, the thermal factor defines mainly the amount of solidifying metal, the metallurgical factor determines the temporal and residual strain/stress evolution, and the metallurgical factor governs the local material properties. On the other hand, all three factors and their interactions are greatly influenced by the shape of the weld pool and vice versa, as shown in [11]. Early research on deep penetration electron beam welding proved the importance of this dependency experimentally by introducing a pure Ni wire at different points throughout the thickness of the specimen to visualize the solidification front in the longitudinal section after the welding process. Thereby, a local disturbance of the solidification front was seen in the longitudinal section. This disturbance, nowadays known as the bulging effect, caused a locally delayed solidification, which led to a further increase of the cracking sensitivity [12–15]. To the best of the authors' knowledge, there are just a few published studies on the occurrence of the bulging effect, i.e., the broadening of the weld pool interface during welding with high-power lasers. To overcome the limited experimental accessibility and capture the formation and evolution of the bulging region, state-of-the-art visualization techniques combining quartz glass with high-speed photography and thermal camera recording have been used in more recent research [11,16]. In [17,18] the authors made attempts to measure and quantify the extent of bulging during hybrid laser gas metal arc welding by establishing an angle based on the narrowest and widest cross-sectional dimensions inside the bulging region. Although recent research shows that the bulging effect occurs during laser beam welding of thick steel sheets, the collected data does not allow for a comprehensive study of the weld pool widening, such as the study of its formation mechanisms or its impact on critical factors for defect formation. On the other hand, numerical simulations have provided major insights into the research of complicated processes as computational capacity has improved in the past two decades. The bulging effect can be discovered in various numerical publications, including [19–25], although not being the subject studied therein. In [7,26], its impact on the mechanical factor, i.e., on the temporal strain/stress evolution in the center of the bulging region, has been investigated. The equivalent heat source (EHS) technique, see, e.g., [27], has been used to further enhance this study, [28,29]. The EHS method allows for a precise coupling of the weld pool shape anticipated by a weld pool dynamics simulation and subsequent thermo-mechanical calculations [30,31]. The authors' earlier research [32] provides an overview of the relationship between the bulging effect and the occurrence of hot cracks during complete penetration laser beam welding, taking into account the three main factors. The authors focus on the interplay between the bulge and the increased solidification temperature range caused by segregation of impurities, such as sulfur and phosphorous, leading to their aggregation ahead of the solid-liquid interface. It has already been shown in [33,34], that such a solidification delay reduces the welded components' cracking resistance.

According to the state-of-the-art in the literature, the bulging effect plays a critical role in the formation of defects during complete penetration laser beam welding. However,

most of the numerical works on this subject either ignore the bulging phenomenon completely or focus on its phenomenological reproduction in order to predict its impact on critical factors such as the three main factors determining the specimens' cracking susceptibility. As a result, a more in-depth numerical analysis of this phenomenon is required to comprehend the formation of the bulging during laser beam welding process and select appropriate process parameters. The current research focuses on the formation of the bulge and specifically its relationship to the weld penetration depth. Therefore, an effort is made to develop a three-dimensional transient multiphysics numerical model that considers the most important physical phenomena, including the multiple reflections and Fresnel absorption on the keyhole surface, the vaporization effects, the thermo-capillary, and natural convection, the latent heat of phase transformations, and the temperature-dependent material properties up to the evaporation temperature. Moreover, a large amount of experimental data is collected to verify the model's predictions.

METHODOLOGY

MATERIALS

In the welding experiments, two types of unalloyed steel sheets with varying thicknesses were used: 8 mm thick high strength steel sheets for ship structures EH36-N and 12 mm thick structural steel sheets S355J2+N. The EH36-N and S355J2+N sheets had dimensions of 300 mm x 100 mm x 8 mm and 175 mm x 100 mm x 12 mm, respectively. The chemical compositions of the materials used was determined by spectral analysis and are listed in Table 1. Note that the amount of P and S in the steel sheets is very low and therefore the maximum values from the corresponding standard were used in the model.

Table 1 Measured and standardized chemical composition of the materials used in wt%.

Material	C	Si	Mn	P	S	Cu	Fe
EH36-N	0.260	1.400	0.028	-	-	0.012	bal.
S355J2+N	0.088	0.34	1.38	-	-	0.028	bal.
DIN EN 10025	≤0.2	≤0.55	≤1.6	≤0.025	≤0.035	≤0.55	bal.

EXPERIMENTS

The technical equipment in the experiments included a Trumpf 16002 disc laser with a 16 kW diode laser illumination, and a Photron FASTCAM SA4 high-speed camera, and thermocouples of type K.

The experimental setup is depicted in Fig. 1, and the process parameters are listed in Table 2. All welds produced in the experiments were bead-on-plate welds. The high-speed camera's frame rate was set to 1000 frames per second, and the diode laser power to 200 W.

The experiments were separated into three steps in total. In the first step, a drilling time estimation for the complete penetration welding on EH36-N sheets was obtained.

Thereby, the optical axis of the high-speed camera lens was aligned perpendicularly to the longitudinal section of the sheet. As a result, the first laser reflection on the top surface can be captured, as well as the moment when the keyhole penetrates the full thickness of the workpiece. In addition, as indicated in Fig. 2 a), thermocouples were placed along the weld centerline. One thermocouple was placed on the top surface of the specimen and used as a trigger. Additionally, three thermocouples were placed on the bottom surface with a distance of around 5 mm to measure the thermal cycle. The moment of complete penetration has been estimated based on the measured time temperature curves. To acquire an accurate averaged value of the drilling period, the experiment was repeated three times.

In the second step of the experiments, the partial penetration welding on the same specimens was performed. Thereby, the weld pool length on the top surface was recorded by the high-speed camera, and the thermal cycles were measured by thermocouples located at different distances from the weld centerline, see Fig. 2 b). The thermocouples utilized in the study were of type K and had a diameter of 0.25 mm.

In the last step, the 12 mm thick S355J2+N sheets were welded. For the sheets welded in the second and third step of the experiment, macro sections were taken from the highlighted locations in Fig. 2 c). Several metallographic cross-sections were obtained using a 2% nital etching. These were subsequently compared to the numerically obtained results.

Table 2 Processing parameters of the experiments.

| Parameters		Value	
Wave length		1030 nm	
Fibre diameter		200 µm	
Beam parameter product (BPP)		8 mm mrad	
Focal diameter		500 µm	
Focal length		300 mm	
Material		EH36-N	S355J2+N
Penetration	partial	complete	partial
Sheet thickness	8 mm	8 mm	12 mm
Laser power	5 kW	8 kW	8 kW
Focal position		0 mm	
Welding speed		2 m min^{-1}	
Laser torch angle		0°	
Shielding gas nozzle angle		35°	
Shielding gas		Ar, 25 L min^{-1}	
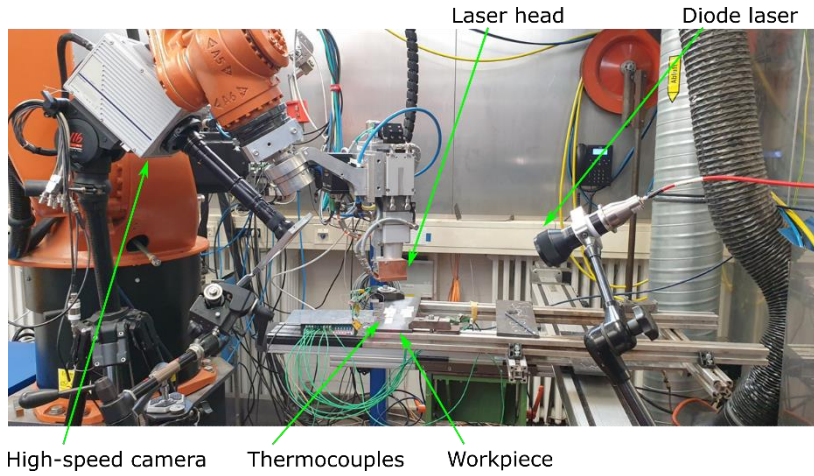
Fig. 1 Experimental setup
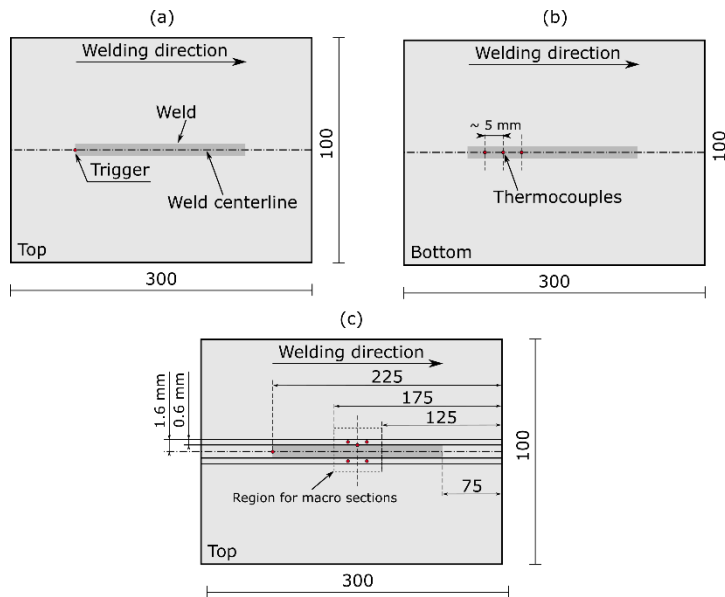
Fig. 2 Overview of the positions of the thermocouples for the measurement of the: a)-b) laser drilling time and c) time-temperature curves

For the objective of improving the level of understanding regarding the formation of a bulging region, a three-dimensional thermo-fluid dynamics model taking into consideration the free surface tracking by the volume of fluid (VOF) approach has been developed. The numerical framework is based on previous works published in [35–39], with some additional enhancements and modifications.

Assumptions

Despite the fact that more complex problems may nowadays be numerically analyzed due to the advances in computing power, substantial simplifications still need to be made in order to get the computational results in a reasonable amount of time. The complex physics behind the laser beam welding process, which includes a variety of strongly coupled, highly nonlinear interactions between the laser radiation, the vapor phase, the molten metal, and the solid material, is another reason for the model's simplifications. The following are the primary assumptions used in the simulation:

- The molten metal is assumed to be Newtonian and incompressible, whereby the flow regime of the liquid metal is considered to be laminar.
- The evaporation of the metal and the vapor flow are not considered in the model. Instead, an empirical model is used to account for the effect of the vapor phase on the surface of the keyhole.
- The impact of the density deviation on the flow due to the temperature difference is modeled using the Boussinesq approximation.

Governing equations

In the following, the governing equations that describe the multiphysics model in a fixed Cartesian coordinate system are given. The transient deformation of the solidified weld seam profile and molten pool free surface is modeled using the VOF technique.

- Volume fraction conservation

$$\frac{\partial \alpha_{vol_{steel}}}{\partial t} + \nabla \cdot \left(\vec{v} \alpha_{vol_{steel}} \right) = 0, \tag{1}$$

where $\alpha_{vol_{steel}}$ denotes the volume fraction of the steel phase in a control volume and $\vec{v} = (u, v, w)$ is the fluid velocity vector. There are three possible conditions for the control volume defined by the volume fraction of the steel, namely a control volume containing only the air phase, $\alpha_{vol_{steel}} = 0$, a control volume containing only the steel phase, $\alpha_{vol_{steel}} = 1$, and a mixture control volume containing the interface between the steel and the air phases, $0 < \alpha_{vol_{steel}} < 1$. Note that the volume fraction conservation equation is solved only for the steel phase; the volume fraction of the air phase is computed based on the following constraint:

$$\sum_{i=1}^{2} \alpha_{vol_i} = 1, \tag{2}$$

where the subscript, $i = 1$, denotes the steel phase and, $i = 2$, the air phase [40]. A piecewise-linear approach is used to reconstruct the steel-air interface, based on the assumption that the interface has a linear slope within each control volume [41]. Volume fraction values between 0.2 and 1 and an empirically determined critical volume fraction gradient value are used to approximate the free surface of the molten pool and the solidified weld.

- Mass conservation

$$\nabla \cdot \vec{v} = 0. \tag{3}$$

- Momentum conservation

Throughout the computational domain, a single momentum equation is solved. The material parameters in each cell are averaged by the volume fraction as a consequence, and the resulting velocity field is shared among the phases. For instance, the density is determined as follows:

$$\rho_{mix} = \alpha_{vol_{steel}}\rho_{steel} + \left(1 - \alpha_{vol_{steel}}\right)\rho_{air}, \tag{4}$$

where ρ_{mix} is the volume-fraction-averaged density; ρ_{air} and ρ_{steel} are the densities of the air and steel phases, respectively. This method is used to calculate all remaining properties such as viscosity and thermal conductivity except the thermal expansion coefficient. The momentum equation is given as follows:

$$\rho_{mix}\left(\frac{\partial \vec{v}}{\partial t} + (\vec{v} \cdot \nabla)\vec{v}\right) = -\nabla p + \mu_{mix}\nabla^2\vec{v} + \rho_{mix}\vec{g} + \vec{S}_m, \tag{5}$$

where t is the time, p is the fluid pressure, μ_{mix} is the dynamic viscosity, $\vec{g}$ is the gravitational acceleration vector, and $\vec{S}_m$ is the momentum source term, which is expressed as follows:

$$\vec{S}_m = -\rho_{steel}\vec{g}\beta_{steel}(T - T_{liq}) + \frac{\left(1 - \alpha_{liq}\right)^2}{\left(\alpha_{liq}^3 + \epsilon\right)}A_{mush}\vec{v}$$
$$+\vec{S}_{surf.tension} + \vec{S}_{rec} + \vec{S}_{vapor}, \tag{6}$$

where β_{steel} is the thermal expansion coefficient, T is the temperature, T_{liq} is the liquidus temperature of the unalloyed steel taken as the reference temperature here, α_{liq} is the liquid volume fraction, ϵ is a small number in the order of 1×10^{-3}, used to avoid division by zero, and A_{mush} is the mushy zone constant.

The thermal buoyancy caused by changes in steel density with temperature is described by the first term on the right-hand side (RHS) of Eq. (6) [42]. The second term on the RHS relates the inverse of the size of the interdendritic structure to the loss of momentum due to solidification in the mushy zone. Thereby, the mushy zone constant A_{mush} is a measure for the amplitude of the damping, thus it should be very large to allow for a steeper transition of the velocity of the liquid metal to zero as it solidifies, in the current study a value in the order of 1×10^7 kg m^{-3} s^{-1} was chosen [43,44]. The liquid fraction α_{liq} is defined as:

$$\alpha_{liq} = \begin{cases} 0 & \text{for } T < T_{sol} \\ \frac{T-T_{sol}}{T_{liq}-T_{sol}} & \text{for } T_{sol} \leq T \leq T_{liq,} \\ 1 & \text{for } T > T_{liq} \end{cases} \tag{7}$$

where T_{sol} denotes the solidus temperature of the material used. Additionally, the flow in the mushy zone is modeled using the effective viscosity approach. As a result, the coherent solid fraction $F_c = 0.48$ and the critical solid fraction $F_{cr} = 0.64$ are used to divide the mushy zone into three subregions. However, each region has a different local viscosity and drag coefficient. The local effective viscosity is expressed as a function of the solid fractions [45]:

$$\mu_{steel} = \mu_0 \left(1 - \frac{F_s}{F_{cr}}\right)^{-1.55}, \quad \text{for} \quad F_s \neq F_{cr}, \tag{8}$$

where μ_0 is the dynamic viscosity at T_{liq} and F_s is the solid fraction. Thereby, a value of 200 Pa s was chosen for the local viscosity in control volumes with a solid fraction higher than the critical solid fraction. The effects of surface tension at the steel-air interface are included in the third term of Eq. (6). Thus, the Marangoni stress resulting from the fluctuation in surface tension is calculated as follows:

$$\tau_{Ma} = \frac{\partial \gamma}{\partial T} \frac{\partial T}{\partial \vec{t}}, \tag{9}$$

where γ is the surface tension and $\vec{t}$ is the surface unit tangential vector. The surface tension is approximated according to [46]:

$$\gamma = \gamma_0 - \hat{A}(T - T_{liq}) - R_g T \Gamma_s ln - (1 + K_s a_s)$$
$$\text{with } K_s = k_l \exp\left(\frac{-\Delta H_0}{R_g T}\right), \tag{10}$$

where γ_0 is the surface tension of the pure metal (here iron), $\hat{A}$ is the negative slope of γ as function of the temperature, R_g is the universal gas constant, Γ_s is the surface excess at saturation, a_s is the thermodynamic activity, k_l is a constant related to the entropy of segregation, and H_0 is the standard heat of adsorption. The capillary pressure, which is the differential in pressure along the steel-air interface, is calculated as:

$$p_{ca} = \gamma \kappa, \tag{11}$$

with $\kappa = \nabla \cdot \hat{\vec{n}}$ defined as the curvature in terms of the divergence of the surface unit normal vector, $\hat{\vec{n}} = \frac{\vec{n}}{|\vec{n}|}$; $\vec{n} = \nabla \alpha_{vol_{steel}}$ is the inward surface normal vector defined as the gradient of the volume fraction of the steel phase. The forces acting on the steel-air interface are converted to volume forces using the divergence theorem according to the continuum surface force (CSF) model. Therefore, a transformation term is defined according to [47]:

$$CSF_{momentum} = \frac{\rho_{mix}|\nabla \alpha_{vol_{steel}}|}{\frac{1}{2}(\rho_{air}+\rho_{steel})}, \tag{12}$$

allowing to compute the volume force:

$$\vec{S}_{surf.tension} = (p_{ca}CSF_{momentum})\vec{\hat{n}}. \tag{13}$$

One of the main driving forces on the keyhole surface is the evaporation-induced recoil pressure, which is indicated by the fourth term in Eq. (6). According to [48], the recoil pressure is calculated and converted to a volume force as follows:

$$p_{rec} = \frac{AB_0}{\sqrt{T}} exp\left(-\frac{M_{mol}h_v}{R_g T}\right), \ \vec{S}_{rec} = (p_{rec}CSF_{momentum})\vec{\hat{n}}, \tag{14}$$

where A is a numerical coefficient depending on the ambient pressure and its value is approximately $0.55\sqrt{K}$ for practical applications; B_0 is a vaporization constant, which in the case of iron equals 3.9×10^{12} kg m^{-1} s^{-2}; M_{mol} is the molar mass, and h_v is the latent heat of vaporization. The fifth term on the RHS of Eq. (6) includes empirical formulations of the vapor-induced stagnation pressure p_{vapor} and shear stress τ_{vapor}, based on the assumption of a laminar flow regime within the keyhole [49]. According to [19] these can be approximated as given:

$$p_{vapor} = p_0 + \frac{1}{2}\rho_{vapor}\left|\vec{v}_{\vec{n}}\right|^2, \tag{15}$$

$$\tau_{vapor} = \frac{1}{8}f\rho_{vapor}\left|\vec{v}_{\vec{t}}\right|^2, \tag{16}$$

where p_0 is the vapor or atmospheric pressure, ρ_{vapor} is the metallic vapor density calculated with the ideal gas equation, $\vec{v}_{\vec{n}}$ and $\vec{v}_{\vec{t}}$ are the normal and tangential projections of the vapor velocity vector, $\vec{V}$, on the steel-air interface, respectively, and $f = 64/Re$. The metallic vapor velocity vector acts vertically in the thickness direction and its magnitude at the keyhole entrance is assumed to be 150 m s^{-1} [50]. Additionally, in the partial penetration case, the vapor velocity is defined as a function of the penetration/keyhole depth, h_{depth}, increasing linearly from 0 m s^{-1} at the keyhole bottom to its maximum value at the keyhole entrance. Note that there are two metallic vapor velocity vectors acting in opposite directions in the complete penetration case. Thereby, one vector increases linearly, starting at two-thirds of the plate thickness, reaching 150 m s^{-1} at the keyhole entrance and a second vector increasing in the same manner towards the keyhole exit, reaching 100 m s^{-1} at the sheet bottom [51,52]. The projection of the vapor velocity vector onto the surface unit normal vector, $\vec{\hat{n}}$, of the steel-air interface can be obtained as follows:

$$\vec{v}_{\vec{n}} = \left(\vec{V} \cdot \vec{\hat{n}}\right)\vec{\hat{n}}. \tag{17}$$

The following vector equation can then be used to determine the tangential projection of the vapor velocity:

$$\vec{v}_{\vec{t}} = \vec{V} - \vec{v}_{\vec{n}}. \tag{18}$$

Equation 16 is further simplified by substituting the Re number and f into it:

$$\tau_{vapor} = \frac{8\mu_{Tmax}\left|\vec{v}_{\vec{t}}\right|}{D}, \tag{19}$$

where D is the averaged diameter of the keyhole and $\mu_{T_{max}}$ is the dynamic viscosity at the maximum reachable temperature applied in the model. For the calculation of D, the

keyhole volume, V_{key}, is approximated as a cylindrical pipe with the length of the keyhole depth, h_{depth}, giving:

$$D = \sqrt{\frac{4V_{key}}{h_{depth}\pi}}.$$ (20)

The dynamic viscosity at T_{max} is obtained by making used of the kinematic theory of gases:

$$\mu_{T_{max}} = \frac{M_{mol}}{3\sqrt{2}\hat{\sigma}} \sqrt{\frac{8k_b T_{max}}{\pi M_{mol}}},$$ (21)

where $\hat{\sigma} = \pi d^2_{mol}$ is the collision cross-section of the molecule with the molecular diameter, d_{mol}, and k_b is the Boltzmann constant. The dynamic viscosity value for the unalloyed steel used in this study is approximately 1.62×10^{-4} kg m^{-1} s^{-1} for a super-heating temperature of 3400 K [53,54], as shown in Table 1. The corresponding source term can be expressed as:

$$\vec{S}_{vapor} = \vec{S}_{stagnation} + \vec{S}_{shear},$$

$$\text{with } \vec{S}_{stagnation} = \left(p_{vapor}CSF_{momentum}\right)\vec{\hat{n}},$$ (22)

$$\text{and } \vec{S}_{shear} = \left(\tau_{vapor}CSF_{momentum}\right)\vec{\hat{t}}.$$

Here, the shear stress and stagnation pressure are converted to volume forces using the CSF method, in accordance with [55].

- Energy conservation

$$\rho_{mix}\left(\frac{\partial H_{mix}}{\partial t} + (\vec{v} \cdot \nabla)H_{mix}\right) = \nabla \cdot (\lambda_{mix}\nabla T) + S_e,$$ (23)

where H_{mix} is the enthalpy, λ_{mix} is the heat conductivity, and S_e is the source term. Thereby, the enthalpy of the material is the sum of the sensible enthalpy, h_{mix}, and the latent heat of fusion of the material used, h_f:

$$H_{mix} = h_{mix} + h_f,$$ (24)

with h_{mix}:

$$h_{mix} = h_{ref} + \int_{T_{ref}}^{T} c_{p_{mix}} dT,$$ (25)

where, the subscript, ref, stands for reference and $c_{p_{mix}}$ is the specific heat at constant pressure. Furthermore, the latent heat content, L, in each control volume, is expressed in terms of the latent heat of the material and the liquid fraction:

$$h_f = \alpha_{liq}L,$$ (26)

varying between zero in the solid region and L in the liquid region [43]. The source term can be written as:

$$S_e = S_{laser} + S_{convection} + S_{radiation} + S_{evaporation} + S_{recondensation}.$$ (27)

The laser heat flux density is assumed to have a Gaussian-like axisymmetric distribution defined as [19]:

$$q_L(x, y) = \frac{2P_L}{\pi r_{f0}^2} \exp\left(-2\frac{x^2 + y^2}{r_{f0}^2}\right),$$ (28)

where P_L is the laser power and r_{f0} is the laser beam radius at the focal plane. A self-consistent ray tracing method described in [19] is used to calculate the three-dimensional energy distribution while taking into account the multiple reflections at the keyhole surface and Fresnel absorption. Thereby, the laser beam is approximated with 755 sub-rays, by discretizing the laser spot in the focal plane by 31×31 sub-regions with a length of $D_{sub} = \frac{2r_{f0}}{31}$. Thus, the energy density of each sub-ray is location-dependent. The power of each sub-ray is calculated by multiplying the surface area of the sub-region beneath it by the corresponding sub-ray power density:

$$P_{ray}(x, y) = q_L(x, y)\left(\frac{r_{f0}}{31}\right)^2.$$ (29)

The initial path of each sub-ray is defined by the diffraction of the laser beam. Therefore, the laser beam radius at any height, z, along the optical axis is approximated as:

$$r_f(z) = r_{f0}\left(1 + \left(\frac{z - z_0}{z_r}\right)^2\right)^{1/2}.$$ (30)

Here z_0 is the position of the focal plane and z_r is the Rayleigh length. The reflection direction vector, $\vec{R}_i$, of the i-th reflection is calculated by the following vector equation:

$$\vec{R}_i = \vec{R}_{i-1} - 2(\vec{R}_{i-1} \cdot \hat{n})\hat{n}.$$ (31)

The direct search method described in [56] is used to select the free surface cell from the center of which the sub-ray is reflected. Furthermore, the absorption rate is calculated using the Fresnel reflection model, as stated in [57]:

$$\hat{\alpha} = 1 - \frac{1}{2}\left(\frac{1 + (1 - \varepsilon \cos \theta_i)^2}{1 + (1 + \varepsilon \cos \theta_i)^2} + \frac{\varepsilon^2 - 2\varepsilon \cos \theta_i + 2 \cos^2 \theta_i}{\varepsilon^2 + 2\varepsilon \cos \theta_i + 2 \cos^2 \theta_i}\right),$$ (32)

with ε - a material dependent coefficient taken and modified according to [58] and θ_i - the incident angle at the i-th reflection point. The total energy of all sub-ray reflections in the cell is added up, and the laser power absorbed in each cell is determined by dividing the result by the volume of the cell, V_{cell}:

$$S_{laser}(x, y, z) = \frac{\sum_{j=1}^{755} q_{ray}(x,y)}{V_{cell}}.$$ (33)

The convective and radiative heat transfer are taken into account by the second and third terms on the RHS of Eq. (27), defined as:

$$q_{convection} = h_c(T - T_{ref}),$$

$$q_{radiation} = \sigma \varepsilon_r(T^4 - T_{ref}^4).$$ (34)

Here h_c = 15 W m^{-2} K^{-1} is the heat convection coefficient, σ is the Stefan-Boltzmann constant, and ε_r is the emissivity [59]. Note that it is accounted not only for the outward convective and radiative heat fluxes, but as well for the inward heat fluxes due to the high-temperature metal vapor, reaching temperatures of up to 6000 K, known as a

secondary heat effect. For this, the reference temperature, T_{ref}, was set to 6000 K for the inward heat fluxes, and to 300 K for the computation of the heat loss caused by the outward heat fluxes [60]. In the present study the range of action for the secondary heat effect was adapted according to the geometrical dimensions of preliminary obtained metallographic cross-sections. The evaporation loss source term is calculated according to [61]

$$q_{evaporation} = \rho_{liq} h_v F_e, \tag{35}$$

where ρ_{liq} is the liquid density and F_e is the evaporation recession speed. It should be noted that the evaporation loss was only taken into account for control volumes reaching temperatures higher than 2700 K because the formulation of the evaporation model is derived for rapid evaporation and does not account for diffusive evaporation. Due to the numerical adaptation of the critical temperature value of 2700 K, the overall amount of heat loss falls within the experimentally measured range of up to 3%. The recondensation heat flux is described by the last term on the RHS of Eq. (27). From the total amount of evaporation heat loss, estimated with Eq. (35), 18% are considered as local recondensation, and 72% are linearly redistributed along the keyhole, according to [60]. In the case of complete penetration, the amount is redistributed linearly from zero at the keyhole bottom to its maximum value at the keyhole entrance. On the other hand, in the case of partial penetration, the amount of recondensation heat at the keyhole bottom exit is 80% of the amount at the keyhole top exit. It is important to note that the unit for all heat fluxes mentioned above is W m^{-2}. Therefore, in order to convert the heat fluxes to power densities with the unit of W m^{-3}, a transformation term is defined that is similar to the one applied in the CSF model:

$$TT_{energy} = \frac{\rho_{mix} c_{p_{mix}} |\nabla \alpha_{vol_{steel}}|}{\frac{1}{2}(\rho_{air} c_{p_{air}} + \rho_{steel} c_{p_{steel}})}. \tag{36}$$

Here $c_{p_{air}}$ is the specific heat of air; the resulting power densities are given as:

$$S_i = q_i TT_{energy}, \tag{37}$$

where i stands for convection, radiation, evaporation and recondensation.

Boundary conditions

The pressure and viscous stress boundary conditions on the steel-air interface are expressed by the following scalar conditions in accordance with the fundamentals of fluid dynamics and assuming that the air phase is inviscid ($\mu_{air} = 0$) and incompressible:

$$p_{air} - p_{steel} + 2\mu_{steel} \frac{\partial \vec{v}_{\vec{n}}}{\partial \vec{t}} = p_{ca} + p_{rec} + p_{vapor} \tag{38}$$

$$-\mu_{steel} \left(\frac{\partial \vec{v}_{\vec{n}}}{\partial \vec{t}} + \frac{\partial \vec{v}_{\vec{t}}}{\partial \vec{n}} \right) = \tau_{Ma} + \tau_{vapor}. \tag{39}$$

Note that, as mentioned above, the surface unit normal vector is directed into the steel phase's interior.
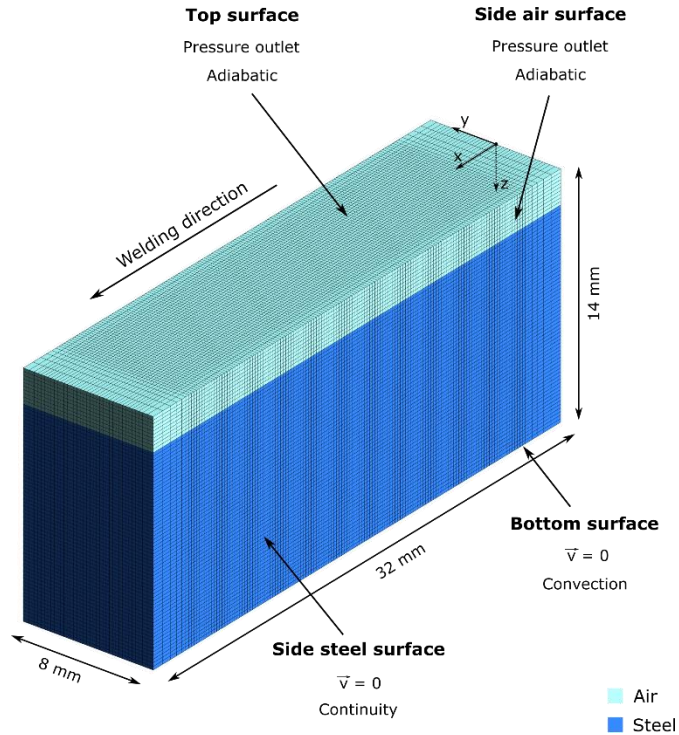
Fig. 3 Overview of the boundary conditions of the multi-physics model

According to the multiple Fresnel absorption, heat convection, thermal radiation, evaporation, and recondensation, the energy boundary condition on the free surface is given as:

$$-\lambda_{mix}\frac{\partial T}{\partial \vec{n}} = q_L - q_{convection} - q_{radiation} - q_{evaporation} + q_{recondensation}. \quad (40)$$

Convective heat transfer was taken into account at the bottom of the steel-phase domain, where the boundaries of the air-phase domain were configured as pressure outlets. It should be noted that the simulation domain was designed to minimize the computing time. As a result, the actual steel sheets are significantly larger than the computational domain. By applying the continuity boundary condition introduced in [62], an appropriate treatment of the boundaries was ensured. The boundary conditions are shown in Fig. 3.

Material properties

The temperature-dependent material properties utilized in the simulation were implemented up to the maximum temperature of 3400 K specified in the model. Because both materials were unalloyed steels, the same thermo-physical material properties were utilized. The base material was modelled as a ferritic phase, with the properties of the

austenite phase being used for temperatures above the austenitization point. The solid-solid phase transformation was considered by converting it to a specific heat and adding this to the heat capacity curve, see Fig. 4. where the thermophysical material properties are plotted. The value for the steel density was averaged in the temperature range of interest between 1200 K and 2800 K, resulting in $\rho_{steel} = 7060$ kg m^{-3}.
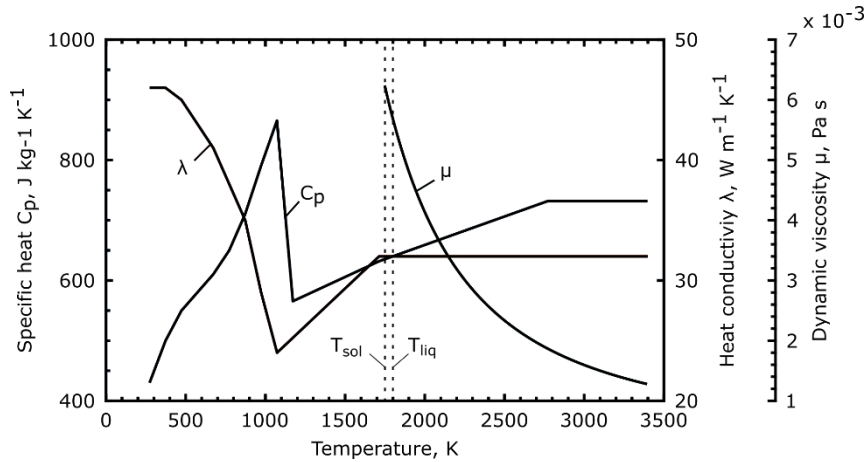

Fig. 4 Thermo-physical material properties for unalloyed steel utilized in the multi-physics model [46,63,64]

Numerical setup

The dimensions of the computational domain used in the present study are 32 mm in length, 8 mm in width, and, depending on the thickness of the steel sheets to be welded, 8 mm or 12 mm in thickness, see also Fig. 3. The regions between -2.9 mm $\leq y \leq 2.9$ mm and 3 mm $\leq x \leq 29$ mm were finely meshed with a recommended fixed cell size of 0.2 mm according to [65]. The cell size outside these regions are defined by a growth rate of 1.1, resulting in a total amount of 372,960 control volumes for the 12 mm thick steel sheets. To ensure an adequate calculation of the reflection point of the sub-rays, the weld seam start and end locations were chosen within the finely meshed region at $x = 3.5$ mm and $x = 28.5$ mm, respectively. Above the steel sheet, an air layer between 0 mm $\leq z \leq 2.0$ mm was defined above the steel sheet allowing to track the free steel-air interface by the VOF method. An identical air layer was put beneath the steel sheet for the full penetration calculation. The finite volume software ANSYS Fluent was used to solve all governing equations. The momentum and energy conservation equations were discretized spatially using a second order upwind technique, and the transient terms were discretized using a first order implicit formulation. The PISO approach was utilized for the pressure-velocity coupling, and the Geo-Reconstruct technique was applied to reconstruct the steel-air interface. The computation was carried out on a high-performance computing cluster at the Bundesanstalt für Materialforschung und -prüfung (BAM). In average, 200 hours computing time were needed to simulate 0.6 second real process time.

RESULTS AND DISCUSSION

VALIDATION OF THE NUMERICAL RESULTS

To validate the numerical results, several experimental data were measured and analyzed in accordance with the ISO/TS 18166 standard [66]. By comparing the averaged drilling time, the weld pool length, the shape of the fusion zone, and the thermal cycles, the multi-physics model was first validated for the 8 mm thick EH36-N sheets. Following the validation of the model, further results, such as for 12 mm thick sheets, were verified by comparing the fusion line and process efficiency.

Comparison of the averaged drilling time

The drilling time was measured using a high-speed camera similar to the experimental setup shown in Fig. 1. To determine an average value for the drilling time at 8 mm thick sheets, the experiment was carried out three times. Table 2 lists the parameters of the process. Two frames recorded by the high-speed camera from one of the three measurements are displayed in Fig. 5. As a result, a) denotes the moment of the first reflection on the top surface of the specimen, and b) the moment when complete penetration is achieved. The measurement tolerance was 1 ms because the frame rate was set to 1000 Hz. The drilling time is calculated from the frames and is approximately 197 ms. The second and third measurements took roughly 164 ms and 224 ms, respectively. In addition, based on the thermocouple values, the drilling time was determined, see Fig. 2 a)-b). Around 7 mm ahead of the welding start point, complete penetration was achieved. The drilling time is estimated to be 210 ms. Thereby, the average of all measurements is 198 ms. The numerically obtained drilling curve is shown in Fig. 5. c). As seen, the drilling time is approximately 191 ms, which agrees well with the experimentally obtained values.
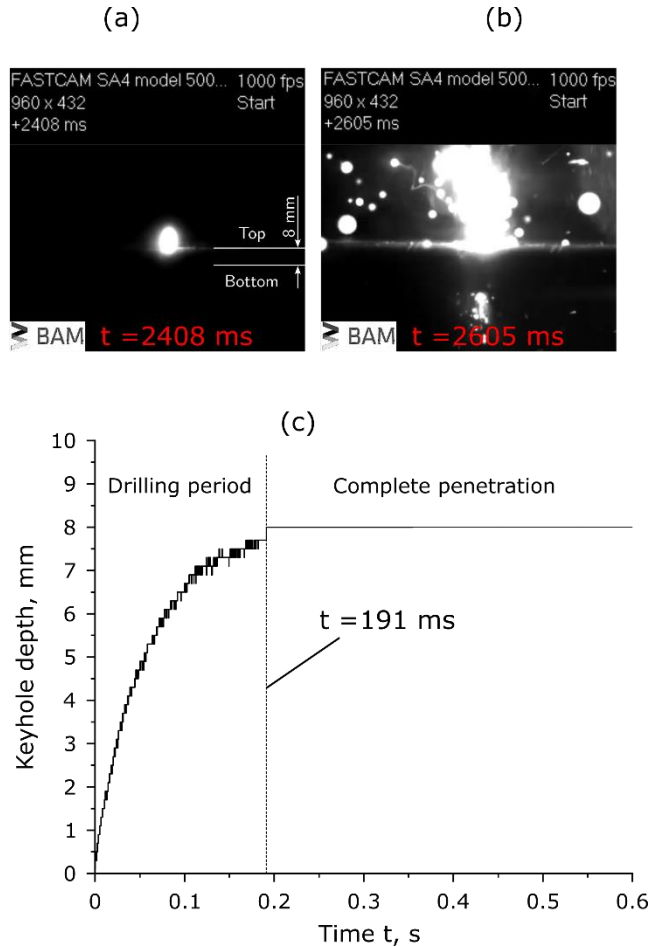
Fig. 5 Drilling time measured by a high-speed camera: a)-b) experimental, c) numerical drilling time

Comparison of the weld pool shape

The precise prediction of the molten pool and the flow pattern therein was one of the objectives of the numerical model. The solidus isotherm, T_{sol}, defines the weld pool interface and enables for the extraction of the numerical fusion line from a cross-section as well as the weld pool length on the top surface. Three metallographic cross-sections were taken from the quasi-steady state region of the weld seam, as shown in Fig. 2, to account for the experimental tolerances c). Fig. 6 a)-c) show the shape of the experimental fusion lines for the 8 mm thick sheets. As illustrated in Fig. 6 d), the experimental tolerance is estimated from the overlap of the three fusion lines. In Fig. 6 e), the numerical fusion line is compared to the experimental average, showing good correlation. The multi-physics model was validated for the partial penetration situation of welding 8

mm thick sheets, as stated above. By comparing the fusion line shape and process efficiency, the numerical figures computed for sheets with a thickness of 12 mm were validated as well. The experimentally measured and numerically estimated fusion lines for the 12 mm thick sheets are shown in Fig. 7. As observed, there are rather small differences between the fusion lines, which are attributable to the experiment and model's tolerances. Finally, the weld pool geometry is verified by comparing the measured and simulated weld pool lengths, as shown in Figure 8. The numerical model predicted an 8.2 mm weld pool length, which was slightly shorter than the experimentally measured value of 8.6 mm. It should be noted that the weld pool length varied along the weld seam. Therefore, a tolerance value is defined as a difference below 5%.
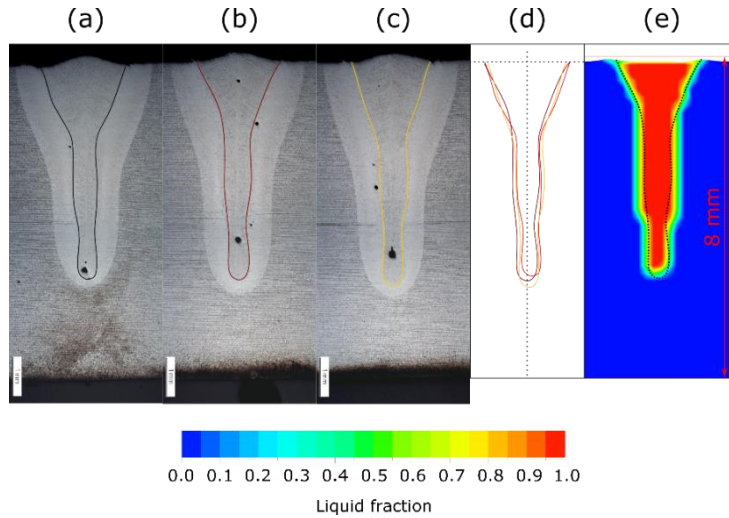

Fig. 6 a)-c) depict three metallographic cross-sections extracted from the middle of the weld seam of the 8 mm thick sheets. Colored lines are used to highlight the fusion line's shape. In d), the overlap of the three fusion lines defines the experimental tolerance range. The fusion line from b) is compared to the calculated fusion line in e)
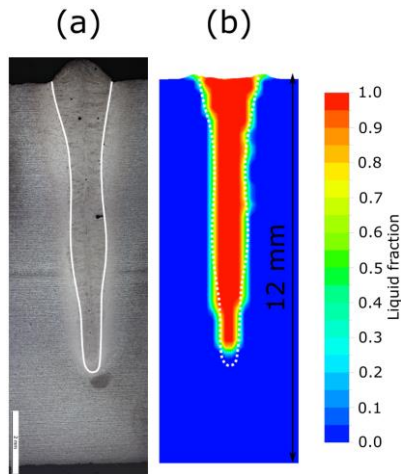
Fig. 7 a) depicts a metallographic cross-section extracted from the middle of the weld seam for 12 mm thick sheets. A white line highlights the fusion line's contour. b) points out the difference between the experimental and numerical fusion lines
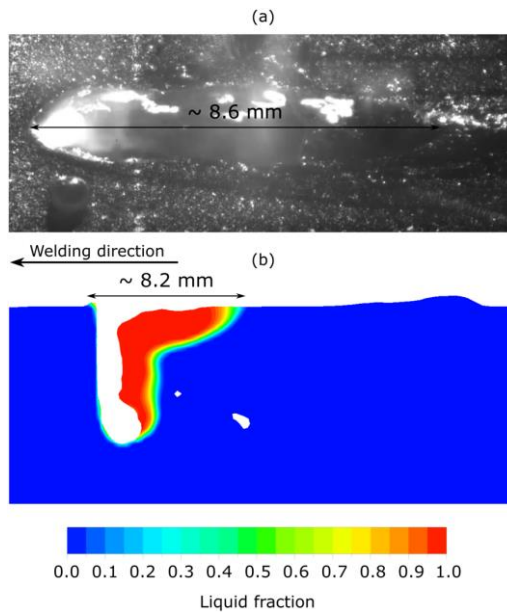

Fig. 8 a) shows the high-speed camera recorded weld pool length from the middle of the weld seam. b) shows the simulated weld pool length at t = 0.33 s

Comparison of the thermal cycles and the process efficiency

The next stage in the validation process is to compare the measured and predicted values for the thermal cycles and process efficiency. The thermal cycles are essential to the welding process because they allow for the prediction of the local microstructure and mechanical characteristics of the component to be joined. The comparison of the measured and calculated time-temperature curves is shown in Fig. 9. Note that a number of time-temperature curves have been obtained experimentally. But for the purposes of comparison, the curve with the highest measured temperature is used. The thermal behavior of the welded sheets is accurately predicted by the numerical model, as shown in Fig. 9. The calculated process efficiency in the model is taken as a validation parameter in addition to the time-temperature curves. The quantity of energy absorbed during the calculations of the complete and partial penetration cases of the 8 mm thick sheets is shown in Fig. 10. The average efficiency in the simulations for both complete and partial penetration was around 79% and 83%, respectively. This agrees well with experimental findings [67] using similar laser powers and processing speeds. It should be noted that the drilling stage of the process was taken into account into the averaged values. The average amount of absorbed energy declines as the process approaches complete penetration at around 200 ms, resulting in a reduced overall averaged amount. The fluctuations of the absorbed heat during partial penetration, on the other hand, are much smaller, caused primarily by fluctuations of the keyhole surface, which have a direct impact on the multiple reflections.
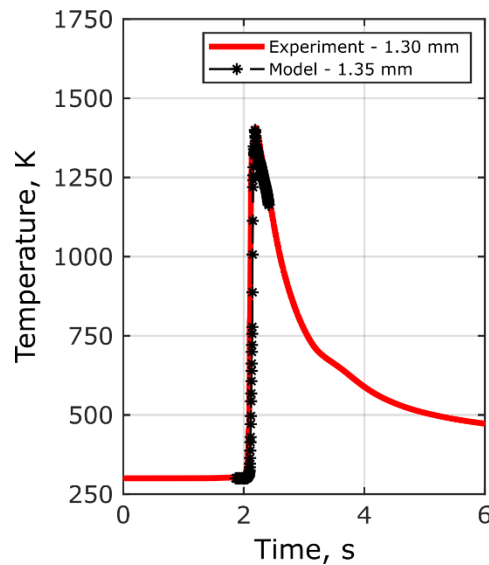

Fig. 9 Comparison of calculated and measured thermal cycles on the top surface of an 8 mm thick sheet
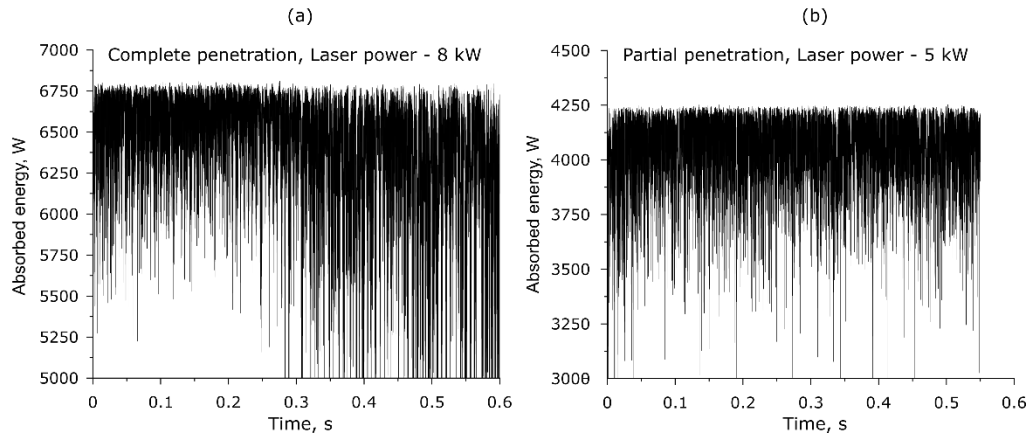
Fig. 10 Amount of absorbed energy computed with the multi-physics model

TRANSITION BEHAVIOR OF THE BULGING EFFECT

The multiphysics model described and validated in the previous sections allowed for the investigation of the fluid flow and thus of the formation of the bulging region. Several experiments and calculations with various sheet thicknesses and welding parameters for the partial penetration case have been carried out in order to estimate the transition from a slight bulge to a fully developed bulging, which can be considered to have a significant impact on the weld seam quality. Based on the numerical results, it was revealed that the flow pattern in the model's longitudinal plane is characterized by two vortexes with opposing directions, regardless of the presence of a bulge region. The thermo-capillary driven flow dominates the upper region of the weld pool, creating an elongated weld pool surface. The weld pool length, as shown in Figs. 11 and 12, is strongly dependent on the dynamic behavior of the keyhole due to transient fluctuations and varies along the penetration depth. The vortex in the lower region of the weld pool is rather small, because of the recoil pressure on the keyhole bottom, which is dependent on the amount of absorbed energy and determined by the multiple reflections in the keyhole. The liquid metal in the upper region flows backwards away from the keyhole rear wall, then downwards and forward in the welding direction at about half the length of the weld pool. The molten material at the bottom is pushed backward and redirected upward along the solid-liquid boundary. The two circulations collide and change course toward the rear wall of the keyhole. The interaction of these circulations contributes to the formation of a bulging region. When the recoil pressure-induced circulation in the bottom part of the weld pool, which pushes the liquid metal to the rear part of the weld pool, and the subsurface backflow in the top region, which is a result of mass conservation, collide, a narrowed zone between these is formed. The narrowing of the weld pool geometry leads to a stronger separation of the two main circulations in the top and bottom region of the weld pool, causing an accumulation of molten material in the bottom region. As a result, a bulging effect is formed.
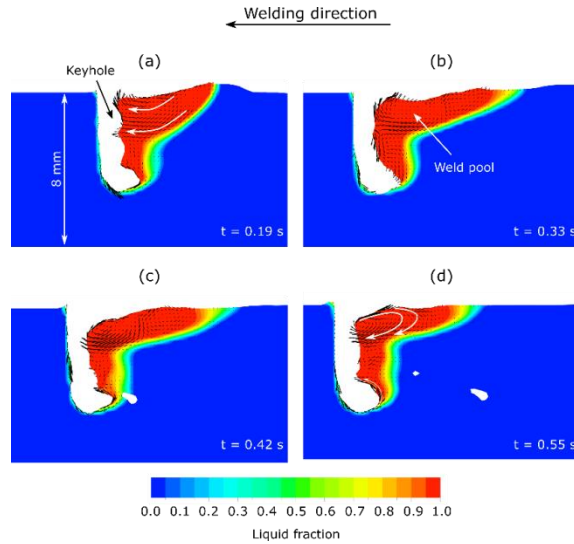
Fig. 11 Temporal evolution of the calculated weld pool shape in the longitudinal plane during partial penetration welding of 8 mm thick sheets
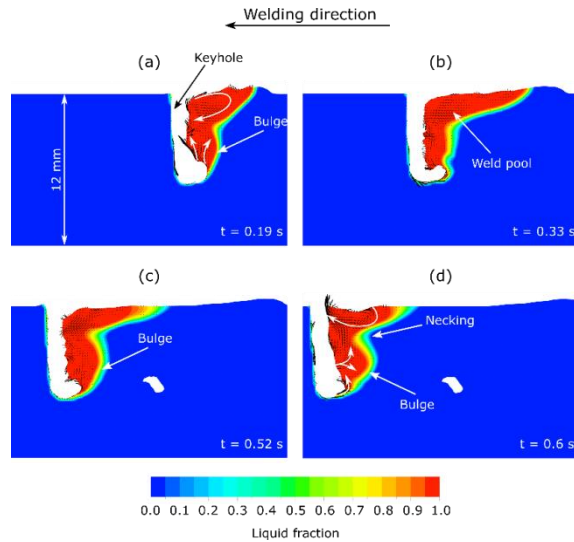

Fig. 12 Temporal evolution of the calculated weld pool shape in the longitudinal plane during partial penetration welding of 12 mm thick sheets

Even though the flow pattern in the weld pool appears to be independent on the bulging region, a bulging region forms when the size and magnitude of the circulations are large enough. The flow directions in the longitudinal section of both the 8 mm and 12 mm thick steel sheets are very similar, as observed in Figs. 11 and 12. In the case of 8 mm thick sheets, however, the two vortexes are not large and strong enough to form a narrowed

region between the top and bottom regions of the weld pool. This statement is as well supported by the experimentally determined depths at which the bulge can be observed in the metallographic cross-sections. According to Figs. 6 and 7, the experimental depths of the center of the bulging region for the 8 mm and 12 mm thick steel sheets are approximately 3.2 mm and 5.2 mm, respectively. As seen in Figs. 11 and 12, these values are in good agreement with the numerically predicted values of 3.8 mm and 4.9 mm. Thereby, the reduced heat input and penetration depth are the cause of the circulations' smaller size and magnitude. The amount of molten material and the penetration depth increase in proportion to the increase in laser power used to weld the 12 mm thick sheets when compared to the case of welding 8 mm sheets. The penetration depth was approximately 5.7 mm and 9.3 mm for the 8 mm and 12 mm sheets, respectively. Thus, as the penetration depth increases, the interaction between the main circulation intensifies, leading to the formation of a necking region between these. The necking forms approximately when the weld pool shape reaches a quasi-steady state, as illustrated in Fig. 12 a). According to numerical observations, both the necking and the bulging are no steady-state phenomena. Although both phenomena are transient, the necking and bulging occur together as if one may be the consequence of the other and vice versa. Moreover, the numerical results show that the bulging occurs at penetration depths above 6 mm and more frequently at penetration depths around 9 mm. Consequently, the region between 6 mm and 9 mm penetration depth can be considered as the transition region from a slight bulge to a fully developed bulge.

CONCLUSIONS

The mechanism of the so-called bulging effect and its transition behavior, or more precisely its dependence on penetration depth, have been confirmed and studied experimentally as well as numerically in the current work. The following are the main conclusions drawn from the obtained results:

- A three-dimensional transient multi-physics numerical model is established, which automatically accounts for the transition from partial to complete penetration welding and allows for the prediction and study of the formation of a bulging region.
- Several experimental measurements and observations, such as drilling time, weld pool length, thermal cycles, process efficiency, and metallographic cross-sections, show very good agreement with the numerically obtained results.
- A bulging region forms once a necking between the top and bottom regions of the weld pool occurs, separating the two main circulations therein. Moreover, the necking and bulging regions are observed to occur transiently but always simultaneously as if one may be the consequence of the other and vice versa.
- It is found that the bulging effect strongly depends on the penetration depth, with an increasing tendency for a bulging region to form with increasing penetration depth. Moreover, the region between 6 mm and 9 mm penetration depth can be considered as the transition region from a slight bulge to a fully developed bulge.

References

[1]   M. BACHMANN, A. GUMENYUK, M. RETHMEIER: 'Welding with high-power lasers: Trends and developments', *Physics Procedia,* 83, pp. 15-25, 2016.

[2]   X. ZHANG, E. ASHIDA, S. TARASAWA, Y. ANMA, M. OKADA, S. KATAYAMA, M. MITZUTANI:'Welding of thick stainless-steel plates up to 50 mm with high brightness lasers', *Journal of Laser Applications*, 23, 2011.

[3]   A. FRITZSCHE, V. AVILOV, A. GUMENYUK, K. HILGENBERG, M. RETHMEIER, M. HIGH: 'Power laser beam welding of thick-walled ferromagnetic steels with electromagnetic weld pool support', *Phys. Procedia*, 83, pp. 362-372, 2016.

[4]   J.F. READY, D.F. FARSON: 'LIA handbook of laser materials processing' *Laser Institute of America*, Orlando, 2001.

[5]   J. SCHUSTER, S. KEITEL, E. SCHULZE, H. MALY: ,Fachbeiträge-entstehung erstarrungsbedingter risse in Laserstrahlschweißverbindungen an unlegierten und niedriglegierten baustahlen', *Schweißen und Schneiden*, 51, pp. 252-257, 1999.

[6]   J. SCHUSTER: ,Heißrisse in Schweißverbindungen: Entstehung, Nachweis und Vermeidung', *DVS-Verlag*, 2004.

[7]   M.O. GEBHARDT, A. GUMENYUK, M. RETHMEIER: 'Numerical analysis of hot cracking in laser hybrid welded tubes', *Advances in Materials Science and Engineering*, 520786, 2004.

[8]   M. RAPPAZ, J. DANTZIG: 'Solidification', *EFPL Press*, first, 2009.

[9]   J. LIPPOLD: 'Welding metallurgy and weldability', *John Wiley & Sons*, 2014.

[10]   C. CROSS: 'On the origin of weld solidification cracking', *Springer*, 3-18, 2005.

[11]   A. ARTINOV N. BAKIR, M. BACHMANN, A. GUMENYUK, M. RETHMEIER: 'Weld pool shape observation in high power laser beam welding' *Procedia CIRP*, 74, pp. 683-686, 2018.

[12]   T. SHIDA, H. OKUMURA, Y. KAWADA: 'Effects of welding parameters and prevention of defects in deep penetration electron beam welding of heavy section steel plates', *Weld. World*, 17, pp. 196-207, 1979.

[13]   S. TSUKAMOTO, H. IRIE, M. INAGAKI: 'Welding defects and molten metal behaviour in electron beam welding', *The fourth international Symposium of the Japan Welding Society*, pp. 115-120, 1982.

[14]   S. TSUKAMOTO, H. IRIE: 'Welding defects and molten metal behaviour in low speed electron beam welding', *Welding in the World*, pp. 130-140, 1985.

[15]   S. TSUKAMOTO, H. IRIE: 'Mechanism of locally delayed solidification in electron beam welding', *Welding international*, 5, pp. 177-183, 1991.

[16]   A. ARTINOV, N. BAKIR, M. BACHMANN, A. GUMENYUK, S.J. NA, M. RETHMEIER: 'On the search for the origin of the bulge effect in high power laser beam welding', *Journal of Laser Applications*, 31, 2019.

[17]   L. BARBETTA, W. WEINGAERTNER, O. SEFFER, R. LAHDO, AND S. KAIERLE: 'Influence of molten pool geometry and process parameters on solidification cracks formation in hybrid laser-GMA welding of thick 5L X70 steel plates', in *ABCM International Congress of Manufacturing Engineering (COBEM),* 8th Brazilian Congress of Manufacturing Engineering, Brazil, pp. 18-22, 2015.

[18]   L.D. BARBETTA, W.L. WEINGAERTNER, O. SEFFER, R. LAHDO, S. KAIERLE: 'Influence of molten pool geometry and process parameters on solidification cracks formation in hybrid

laser-GMA welding of thick 5L X70 steel plates', *ABCM International Congress of Manufacturing Engineering (COBEM)*, 8th Brazilian Congress of Manufacturing Engineering, 2015.

[19] W.-I. CHO, S.-J. NA, C. THOMY, F. VOLLERTSEN: 'Numerical simulation of molten pool dynamics in high power disk laser welding', *Journal of Materials Processing Technology*, 212, pp. 262-275, 2012.

[20] M. BACHMANN, V. AVILOV, A. GUMENYUK, M. RETHMEIER: 'Experimental and numerical investigation of an electromagnetic weld pool support system for high power laser beam welding of austenitic stainless steel', *Journal of Materials Processing Technology*, 214 pp. 578-591, 2014.

[21] M. BACHMANN, V. AVILOV, A. GUMENYUK, M. RETHMEIER: 'Experimental and numerical investigation of an electromagnetic weld pool control for laser beam welding', *Physics Procedia*, 56, pp. 515-524, 2014.

[22] M. SOHAIL, S.-W. HAN, S.-J. NA, A. GUMENYUK, M. RETHMEIER: 'Numerical investigation of energy input characteristics for high-power fiber laser welding at different positions', *International Journal of Advanced Manufacturing Technology*, 80, pp. 931-946, 2015.

[23] F. LU, X. LI, Z. LI, X. TANG, H. CUI: 'Formation and influence mechanism of keyhole-induced porosity in deep-penetration laser welding based on 3d transient modeling', *International Journal of Heat and Mass Transfer*, 90 pp. 1143-1152, 2015.

[24] M. BACHMANN, R. KUNZE, V. AVILOV, M. RETHMEIER: 'Finite element modeling of an alternating current electromagnetic weld pool support in full penetration laser beam welding of thick duplex stainless steel plates', *Journal of Laser Applications*, 28, 2016.

[25] Z. GAO, P. JIANG, G. MI, L. CAO, W. LIU: 'Investigation on the weld bead profile transformation with the keyhole and molten pool dynamic behavior simulation in high power laser welding', *International Journal of Heat and Mass Transfer*, pp.1304-1313, 2018.

[26] M.O. GEBHARDT: 'Einfluss von Konstruktion und Schweißparametern auf die Erstarrungsrissentstehung beim Laser-MSG-Hybridschweißen dickwandiger Bauteile experimentelle und numerische Analyse', *Bundesanstalt für Materialforschung und Prüfung (BAM)*, 2014.

[27] D. RADAJ, H. HÄUSER, S. BRAUN: 'Numerische Simulation von Eigenspannungen und Verzug bei Schweißverbindungen aus AlMgSi-Legierungen', *Konstruktion*, pp. 31-37, 1998.

[28] A. ARTINOV, M. BACHMANN, M. RETHMEIER: 'Equivalent heat source approach in a 3d transient heat transfer simulation of full-penetration high power laser beam welding of thick metal plates', *International Journal of Heat Mass Transfer*, 122, pp. 1003-1013, 2018.

[29] N. BAKIR, A. ARTINOV, A. GUMENYUK, M. BACHMANN, M. RETHMEIER: 'Numerical simulation on the origin of solidification cracking in laser welded thick-walled structures', *Metals*, 8, p. 406, 2018.

[30] A. ARTINOV, V. KARKHIN, N. BAKIR, M. X, M. BACHMANN, A. GUMENYUK, M. RETHMEIER: 'Lam curves approximation for the assessment of the 3-d temperature distribution in keyhole mode welding processes', *Journal of Laser Applications*, 32, 2020.

[31] A. ARTINOV, V. KARKHIN, P. KHOMICH, M. BACHMANN, M. RETHMEIER: 'Assessment of thermal cycles by combining thermo-fluid dynamics and heat conduction in keyhole mode welding processes', *International Journal of Thermal Sciences*, 145, 2019.

[32] A. ARTINOV, M. BACHMANN, X. MENG, V. KARKHIN, M. RETHMEIER: 'On the relationship between the bulge effect and the hot cracking formation during deep penetration laser beam welding', *Procedia CIRP*, 94, pp. 5-10, 2020.

[33] S. KOU: 'Welding Metallurgy', *John Wiley & Sons*, 2003.

[34] M.E. GLICKSMAN: 'Principles of solidification: An introduction to modern casting and crystal growth concepts', *Springer New York*, 2011.

[35] X. MENG, M. BACHMANN, A. ARTINOV, M. RETHMEIER: 'Experimental and numerical assessment of weld pool behavior and final microstructure in wire feed laser beam welding with electromagnetic stirring', *Journal of Manufacturing Processes*, 45, pp. 408-418, 2019.

[36] X. MENG, A. ARTINOV, M. BACHMANN, M. RETHMEIER: 'Numerical and experimental investigation of thermo-fluid flow and element transport in electromagnetic stirring enhanced wire feed laser beam welding', *International Journal of Heat Mass Transfer*, 144, 2019.

[37] X. MENG, A. ARTINOV, M. BACHMANN, M. RETHMEIER: 'Numerical study of additional element transport in wire feed laser beam welding', *Procedia CIRP*, 94, pp. 722-725, 2020.

[38] X. MENG, A. ARTINOV, M. BACHMANN, M. RETHMEIER: 'Theoretical study of influence of electromagnetic stirring on transport phenomena in wire feed laser beam welding', *Journal of Laser Applications,* 32 (2), 2020.

[39] X. MENG, M. BACHMANN, A. ARTINOV, M. RETHMEIER: 'The influence of magnetic field orientation on metal mixing in electromagnetic stirring enhanced wire feed laser beam welding', *Journal of Materials Processing Technology*, 294, 2021.

[40] C.W. HIRT, B.D. NICHOLS: 'Volume of fluid (VOF) method for the dynamics of free boundaries', *Journal of Computational Physics*, pp. 201-225, 1981.

[41] D.L. YOUNGS: 'Time-dependent multi-material flow with large fluid distortion', *Numerical Methods for Fluid Dynamics*, 24, pp. 273-285, 1982.

[42] T.E. FABER: 'Fluid dynamics for physicists', *Cambridge University Press*, 1995.

[43] V.R. VOLLER, C. PRAKASH: 'A fixed grid numerical modelling methodology for convection-diffusion mushy region phase-change problems', *International journal of heat and mass transfer*, 30, pp. 1709-1719, 1987.

[44] A.D. BRENT, V.R. VOLLER, K.T.J. REID: 'Enthalpy-porosity technique for modeling convection-diffusion phase change: application to the melting of a pure metal', *Numerical Heat Transfer*, Part A Applications, 13, pp. 297-318, 1988.

[45] M.H. CHO, Y.C. LIM, D.F: 'Farson, Simulation of weld pool dynamics in the stationary pulsed gas metal arc welding process and final weld shape', *Welding Journal New-York*, 85, pp. 271-283, 2006.

[46] P. SAHOO, T. DEBROY, M.J. MCNALLAN: 'Surface tension of binary metal-surface active solute systems under conditions relevant to welding metallurgy', *Metallurgical transactions B*, 19, pp. 483-491, 1988.

[47] J.U. BRACKBILL, D.B. KOTHE, C. ZEMACH: 'A continuum method for modeling surface tension', *Journal of Computational Physics*, 100, pp. 335-354, 1992.

[48] V. SEMAK, A. MATSUNAWA: 'The role of recoil pressure in energy balance during laser materials processing', *Journal of Physics D-Applied Physics*, 1997.

[49] F.M. WHITE: 'Fluid mechanics froth edition', *McGraw-Hill*, New York, 1999.

[50] E.H. AMARA, A. BENDIB: 'Modelling of vapour flow in deep penetration laser welding', *Journal of Physics D-Applied Physics*, 35, pp. 272-280, 2002.

[51] D. WU, X. HUA, F. LI, L. HUANG: 'Understanding of spatter formation in fiber laser welding of 5083 aluminum alloy', *International Journal of Heat and Mass Transfer*, pp. 730-740, 2017.

[52] R. ZHANG, X. TANG, L. XU, F. LU, H. CUI: 'Study of molten pool dynamics and porosity formation mechanism in full penetration fiber laser welding of al-alloy', *International Journal of Heat and Mass Transfer*, 148, 2020.

[53] W. TAN, N.S. BAILEY, C.S. YUNG: 'Investigation of keyhole plume and molten pool based on a three-dimensional dynamic model with sharp interface formulation', *Journal of Physics D: Applied Physics*, 46, 2013.

[54] W. TAN, C.S. YUNG: 'Analysis of multi-phase interaction and its effects on keyhole dynamics with a multi-physics numerical model', *Journal of Physics D: Applied Physics*, 47, 2014.

[55] G.P. SASMAL: 'Numerical modeling of thermocapillary convection with curved and deforming free surfaces', *Previews of Heat and Mass Transfer*, 5(21), pp. 457-458, 1995.

[56] S.-W. HAN, A. JUNSU, S.J. NA: 'A study on ray tracing method for CFD simulations of laser keyhole welding: progressive search method', *Welding in the World*, 60, pp. 247-258, 2016.

[57] W. SCHULZ, G. SIMON, H.M. URBASSEK, L. DECKER: 'On laser fusion cutting of metals', *Journal of Physics D-Applied Physics*, 20, pp. 481-488, 1987.

[58] R. DUCHARME, K. WILLIAMS, P. KAPADIA, J. DOWDEN, B. STEEN, M. GLOWACKI: 'The laser welding of thin metal sheets: an integrated keyhole and weld pool model with supporting experiments', *Journal of physics D: Applied physics*, 27, p. 1619, 1994.

[59] T.L. BERGMAN, F.P. INCROPERA: 'Fundamentals of heat and mass transfer', *John Wiley & Sons*, 2011.

[60] S. MUHAMMAD, S. HAN, S.J. NA, A. GUMENYUK, M. RETHMEIER: 'Study on the role of recondensation flux in high power laser welding by computational fluid dynamics simulations', *Journal of Laser Application*, 30, 2018.

[61] H. KI, P.S. MOHANTY, J. MAZUMDER: 'Modelling of high-density laser-material interaction using fast level set method', *Journal of Physics D: Applied Physics*, 34, pp. 364-372, 2001.

[62] X. MENG, G. QIN, R. ZONG: 'Thermal behavior and fluid flow during humping formation in high-speed full penetration gas tungsten arc welding', *International Journal of Thermal Science*, 134, pp. 380-391, 2018.

[63] K.C. MILLS: 'Recommended values of thermophysical properties for selected commercial alloys', *Woodhead Publishing*, 2002.

[64] Material database, 2009, ESI Group.

[65] W. I. N. CHO, S.J.: 'Impact, of wavelengths of CO2, disk, and green lasers on fusion zone shape in laser welding of steel', *J. Weld. Join*, 38, pp. 235-240, 2020.

[66] ISO/TS 18166:2016 Numerical welding simulation Execution and documentation.

[67] Y. KAWAHITO, N. MATSUMOTO, Y. ABE, S. KATAYAMA: 'Relationship of laser absorption to keyhole behavior in high power fiber laser welding of stainless steel and aluminum alloy', *Journal of Materials Processing Technology*, 211, pp. 1563-1568, 2011.